



# Dramatic improvement in the “Bulk” hyperpolarization of $^{131}\text{Xe}$ via spin exchange optical pumping probed using *in situ* low-field NMR

Michael J. Molway<sup>a</sup>, Liana Bales-Shaffer<sup>a</sup>, Kaili Ranta<sup>a</sup>, James Ball<sup>b</sup>, Eleanor Sparling<sup>b</sup>, Mia Prince<sup>b</sup>, Daniel Cocking<sup>b</sup>, Dustin Basler<sup>a</sup>, Megan Murphy<sup>a</sup>, Bryce E. Kidd<sup>a</sup>, Abdulbasit Tobi Gafar<sup>a</sup>, Justin Porter<sup>a</sup>, Kierstyn Albin<sup>a</sup>, Matthew S. Rosen<sup>c,d</sup>, Eduard Y. Chekmenev<sup>e,f</sup>, W. Michael Snow<sup>g</sup>, Michael J. Barlow<sup>b</sup>, Boyd M. Goodson<sup>a,\*</sup>

<sup>a</sup> School of Chemical and Biomolecular Sciences, Southern Illinois University, Carbondale 62901, IL, USA

<sup>b</sup> School of Medicine, University of Nottingham, Queens Medical Centre, Nottingham, UK

<sup>c</sup> A.A. Martinos Center for Biomedical Imaging, Massachusetts General Hospital and Harvard Medical School, Boston 02129, MA, USA

<sup>d</sup> Department of Physics, Harvard University, Cambridge 02138, MA, USA

<sup>e</sup> Department of Chemistry, Integrative Biosciences (Ibio), Karmanos Cancer Institute (KCI), Wayne State University, Detroit 48202, MI, USA

<sup>f</sup> Russian Academy of Sciences, Leninsky Prospekt 14, 119991 Moscow, Russia

<sup>g</sup> Department of Physics, Indiana University, Bloomington, IN, USA

## ARTICLE INFO

### Keywords:

Hyperpolarized xenon  
Spin relaxation  
Nuclear physics  
Polarized targets  
TRIV searches

## ABSTRACT

We report on hyperpolarization of quadrupolar ( $I = 3/2$ )  $^{131}\text{Xe}$  via spin-exchange optical pumping. Observations of the  $^{131}\text{Xe}$  polarization dynamics via *in situ* low-field NMR show that the estimated alkali-metal/ $^{131}\text{Xe}$  spin-exchange rates can be large enough to compete with  $^{131}\text{Xe}$  spin relaxation.  $^{131}\text{Xe}$  polarization up to  $7.6 \pm 1.5\%$  was achieved in  $\sim 8.5 \times 10^{20}$  spins—a  $\sim 100$ -fold improvement in the total spin angular momentum—potentially enabling various applications, including: measurement of spin-dependent neutron- $^{131}\text{Xe}$  s-wave scattering; sensitive searches for time-reversal violation in neutron- $^{131}\text{Xe}$  interactions beyond the Standard Model; and surface-sensitive pulmonary MRI.

## 1. Introduction

Spin exchange optical pumping (SEOP) [1] can polarize macroscopic amounts of  $I=1/2$  nuclei like  $^3\text{He}$  and  $^{129}\text{Xe}$  [2–8] to near-unity values [9,10] for applications in biomedical imaging, NMR spectroscopy, and fluid dynamics [11–13], as well as nuclear/particle physics efforts to constrain CPT/Lorentz violations [14–19] and electric dipole moment searches [20]. If  $^{131}\text{Xe}$ —the other stable xenon isotope with non-zero spin—can be sufficiently hyperpolarized, its unique properties may enable new envisioned applications, varying from novel tests of fundamental symmetries to biomedical imaging (respectively exploiting specific neutron resonances and contrast mechanisms that are absent with  $^{129}\text{Xe}$ ). However, the strong quadrupole moment of  $I=3/2$   $^{131}\text{Xe}$  gives rise to much faster spin–lattice relaxation ( $T_1$ ) losses with increasing Xe density and surface interactions [21–23]. This physics has severely constrained the utility of  $^{131}\text{Xe}$  for many applications, even when employing small amounts ( $\lesssim 10^{16}$  spins) of polarized ground state  $^{131}\text{Xe}$

nuclei [24–28,22,29–35] to understand the atomic physics of the SEOP process [24,25], probe gas/surface interactions [26–28,22], study Berry geometric phases [29], or perform  $^{129}\text{Xe}/^{131}\text{Xe}$  comagnetometry [32–35]—including searches for axion-like particles [32]; minute amounts of polarized  $^{131m}\text{Xe}$  [36] have also been used to demonstrate a new MRI/gamma-ray imaging modality [37]. Although larger amounts of hyperpolarized (HP)  $^{131}\text{Xe}$  may be produced transiently via cross-polarization with HP  $^{129}\text{Xe}$  in cryogenic lattices [38], arguably the greatest success with bulk production of HP  $^{131}\text{Xe}$  to date [23] was part of pioneering work by Meersmann and co-workers to hyperpolarize quadrupolar noble gases via SEOP [39–42]. They reported  $^{131}\text{Xe}$  polarizations of 2.2%, 0.44%, and 0.026% at 9.4 T for 0.075, 0.3, and 1.4 bar Xe, respectively, following gas separation from a  $\sim 72$  mL SEOP cell [23].

Here we investigate the preparation of hyperpolarized  $^{131}\text{Xe}$  using isotopic enrichment, next-generation spectrally-narrowed laser diode arrays, and *in situ* low-field NMR to permit real-time observation of

\* Corresponding author.

E-mail address: [bgoodson@chem.siu.edu](mailto:bgoodson@chem.siu.edu) (B.M. Goodson).

<https://doi.org/10.1016/j.jmr.2023.107521>

Received 12 April 2023; Received in revised form 4 July 2023; Accepted 6 July 2023

Available online 10 July 2023

1090-7807/© 2023 Elsevier Inc. All rights reserved.

polarization dynamics and SEOP optimization. The resulting alkali-metal/ $^{131}\text{Xe}$  spin-exchange rates were found to be comparable to the rapid  $^{131}\text{Xe}$  spin relaxation rates in glass cells (estimated using a model).  $^{131}\text{Xe}$  polarization values as high as  $7.6\% \pm 1.5\%$  were achieved at 0.37 amagat<sup>1</sup> in a 0.1 L cell ( $N = 8.5 \times 10^{20}$   $^{131}\text{Xe}$  spins). This approach, here yielding a  $\sim 100$ -fold improvement in  $P_{Xe}N$  (where  $P_{Xe}$  is the nuclear polarization and  $N$  is the number of polarized  $^{131}\text{Xe}$  nuclei), has since enabled the first measurement of the spin-dependent scattering length of polarized neutrons from polarized  $^{131}\text{Xe}$  nuclei [43]. We conclude this paper with a brief discussion of potential applications, including surface-sensitive biomedical imaging and searches for time-reversal invariance violation (TRIV) in polarized neutron transmission at the 3.2 eV p-wave neutron-nucleus resonance in polarized  $^{131}\text{Xe}$ . As detailed in the [Supplemental Information](#) (SI) document, such an experiment could discover new TRIV sources beyond the Standard Model.

## 2. Experimental methods

All SEOP cells were custom-made from Pyrex by Mid-Rivers Glassblowing (Saint Charles, MO), with stopcock assemblies (Chemglass) welded as side-arms to permit loading of contents; [Fig. 1A](#). Unless stated otherwise, all data were taken from uncoated cylindrical ( $2'' \times 2''$ , i.e. 5.08 cm i.d.  $\times$  5.08 cm long) cells ( $V \approx 103 \text{ cm}^3$ ); the lack of hydrophobic coatings, combined with the cell geometry (i.e. with reduced S/V ratio) and high cell temperatures, helped minimize  $^{131}\text{Xe}$  relaxation contributions from surface interactions. [Fig. 1A](#) also shows a “standard” 10" long cell (500 cc [9,10]). Cells were loaded with a small droplet (few hundred mg) of either Rb or Cs in an  $\text{N}_2$ -atmosphere glovebox. A thin alkali metal film was distributed on the cell's side walls with a heat-gun. Cells were then loaded with gas (unless stated otherwise, 300 torr isotopically enriched  $^{131}\text{Xe}$  (84.4%, Berry and Associates/ Icon Isotopes) and 300 torr ultrapure  $\text{N}_2$ ).

A given cell was mounted in either a 3D-printed polycarbonate [44] or home-built Garolite forced-air oven ([Fig. 1B,C](#)); maximum temperatures were 135 °C and 225 °C, respectively. Cell temperature was monitored using a thermocouple fixed to the exterior cell wall using Kapton tape, providing feedback for a temperature controller. The oven was mounted within the homogeneous region of the magnetic field generated by a 22" Helmholtz coil (HC) pair ([Fig. 2](#)).  $^{131}\text{Xe}$  or  $^{129}\text{Xe}$  polarization was monitored *in situ* using a low-field NMR spectrometer (Magritek Aurora, nominal  $^{131}\text{Xe}$  NMR frequency: 20.9, 46, or 66 kHz, corresponding to magnetic fields of approximately 60, 130, or 190 G, respectively) connected to a 1" diameter surface RF coil mounted to the bottom of the cell ([Fig. 2](#)).

For most of the work presented here, optical pumping was performed using one of three lasers tuned to the D1 line of Rb (794.8 nm) or Cs (894.3 nm). Each design uses volume holographic gratings to spectrally narrow the laser output. Before being directed into the SEOP cell, the output of each laser was expanded and rendered circularly polarized using a polarizing beam-splitter cube and quarter-wave plate. For Rb, the first laser was a  $\sim 150$  W microchannel-cooled (MCC) laser (QPC Lasers) with spectral width (defined by the full width half maximum, FWHM) of 0.29 nm. When the Rb/ $^{131}\text{Xe}$  cell was first created, it was found that this laser deposited too much heat into the cell for stable SEOP above  $\sim 90$  °C; thus, the laser's optical train was fitted with a 3" expander and the widened beam was partially blocked with a 1.75" (4.4 cm) aperture, reducing the power on cell to  $\sim 100$  W. Later Rb/ $^{131}\text{Xe}$  SEOP experiments were performed with an Ultra-500 QPC laser with FWHM of 0.18 nm operated between 130–145 W (2" (5.1 cm) beam diameter). All reported Cs/ $^{131}\text{Xe}$  experiments used an OptiGrate ultra-

narrow laser with  $\sim 50$  pm FWHM (power on cell:  $\sim 50$  W).

For some experiments, the spectral profile of near-IR light transmitted through the cell was monitored via fiber optic mounted behind a retro-reflecting mirror. The fiber optic was connected to an Ocean Optics near-IR spectrometer (HR2000 or HR4000,  $\sim 0.04$  nm resolution). Please see Refs. [7,45] for other apparatus details.

## 3. Results and discussion

### 3.1. $^{131}\text{Xe}$ polarization dynamics

[Figs. 3\(a,b\)](#) show time-dependent *in situ*  $^{131}\text{Xe}$  NMR spectra during SEOP with Rb (a) or Cs (b). Use of isotopically enriched  $^{131}\text{Xe}$  and high resonant photon fluxes enabled single-shot  $^{131}\text{Xe}$  detection, improving on previous work [46] and permitting optimization of  $^{131}\text{Xe}$  SEOP and monitoring of  $^{131}\text{Xe}$  polarization dynamics as a function of temperature for each metal ([Figs. 3\(c,d\)](#)). The signals were fit to  $S(t) = S_0[1 - \exp(-t\Gamma_{SEOP})]$  to extract the polarization rate constant for each curve,  $\Gamma_{SEOP}$ .

Resulting  $\Gamma_{SEOP}$  values ([Fig. 4\(a\)](#)) have contributions from alkali-metal/ $^{131}\text{Xe}$  spin-exchange and  $^{131}\text{Xe}$  nuclear spin relaxation:  $\Gamma_{SEOP} = \gamma_{SE} + \Gamma_{Xe}(131)$ , where  $\gamma_{SE}$  is the spin-exchange rate and  $\Gamma_{Xe}(131) = 1/T_1(^{131}\text{Xe})$ . As with  $^{129}\text{Xe}$ , higher alkali metal densities (i.e. higher cell temperatures) increase  $^{131}\text{Xe}$  polarization rates according to the relation  $\gamma_{SE} = \gamma'[\text{Rb}]$ , where  $\gamma'$  is the effective spin-exchange cross section [47]. Here, we are interested in three specific aspects: (1) the absolute magnitude of the spin-exchange rates—and if possible, the magnitudes of the SE cross-sections themselves—for  $^{131}\text{Xe}$  (and their relative sizes compared to corresponding rates of relaxation for  $^{131}\text{Xe}$  and spin-exchange for  $^{129}\text{Xe}$ ), to determine the viability of using SEOP to prepare bulk hyperpolarized  $^{131}\text{Xe}$  for envisioned Neutron Optics Parity and Time Reversal EXperiment (NOPTREX) efforts [48] or other applications; (2) to inform future modeling of  $^{131}\text{Xe}$  SEOP; and (3) to compare the spin exchange attained with a given alkali metal.

Aspects of nuclear spin relaxation and SEOP of different xenon isotopes have long been of fundamental interest (e.g. Refs. [23,49,50,24,25,1,51,52,31,36,47,53–55]). As early examples, Volk and co-workers [24,25] pointed out that one can use the theory of Herman [50]—originally developed to calculate contributions to Rb/gas spin exchange from scalar versus classical dipolar hyperfine interactions—to predict the ratio of spin-exchange cross sections (and hence, the relative sizes of spin-exchange rates) for a given alkali metal with  $^{131}\text{Xe}$  versus  $^{129}\text{Xe}$ :

$$\frac{\gamma'_I}{\gamma'_K} = \frac{I(I+1)\gamma_{I(K)}^2}{K(K+1)\gamma_{K}^2} \approx 2.28, \quad (1)$$

where  $I, K$  are the nuclear spins and  $\gamma_{I(K)}$  are the corresponding gyromagnetic ratios. Thus while simplistic, this would predict  $\sim 2$ -fold lower spin-exchange rates for  $^{131}\text{Xe}$  versus the now-better-characterized values for  $^{129}\text{Xe}$  (e.g. Refs. [1,49,51,52,56,47,57,58]). Yet Volk and co-workers reported an experimental  $\gamma'$  value for Rb/ $^{131}\text{Xe}$  (in cells with only 0.5 torr of enriched  $^{131}\text{Xe}$ ) that was  $\sim 16$ -fold smaller than that measured (separately) for Rb/ $^{129}\text{Xe}$ —an initial result that was rationalized as possibly originating from a hypothesized additional (e.g. quadrupolar) interaction that reduces the efficiency of spin exchange for  $^{131}\text{Xe}$  [24]. However, later experiments from the same group and by Mehring and co-workers (who studied gases with somewhat higher densities—13 mbar and 150 mbar of Xe and  $\text{N}_2$ ) indicated  $\sim 4$ -fold and  $\sim 8$ -fold ratios, respectively [25,22]).  $^{131}\text{Xe}$  spin-exchange rates are practically important for the envisioned TRIV experiments: Given the much greater relaxation rates for  $^{131}\text{Xe}$  versus  $^{129}\text{Xe}$ , a large concomitant reduction in  $\gamma_{SE}$  values could impact the feasibility of bulk hyperpolarized  $^{131}\text{Xe}$  production.

<sup>1</sup> 1 amagat (amg) =  $2.6873 \times 10^{19} \text{ cm}^{-3}$ , equal to the number density of an ideal gas at 0 °C and 760 Torr.

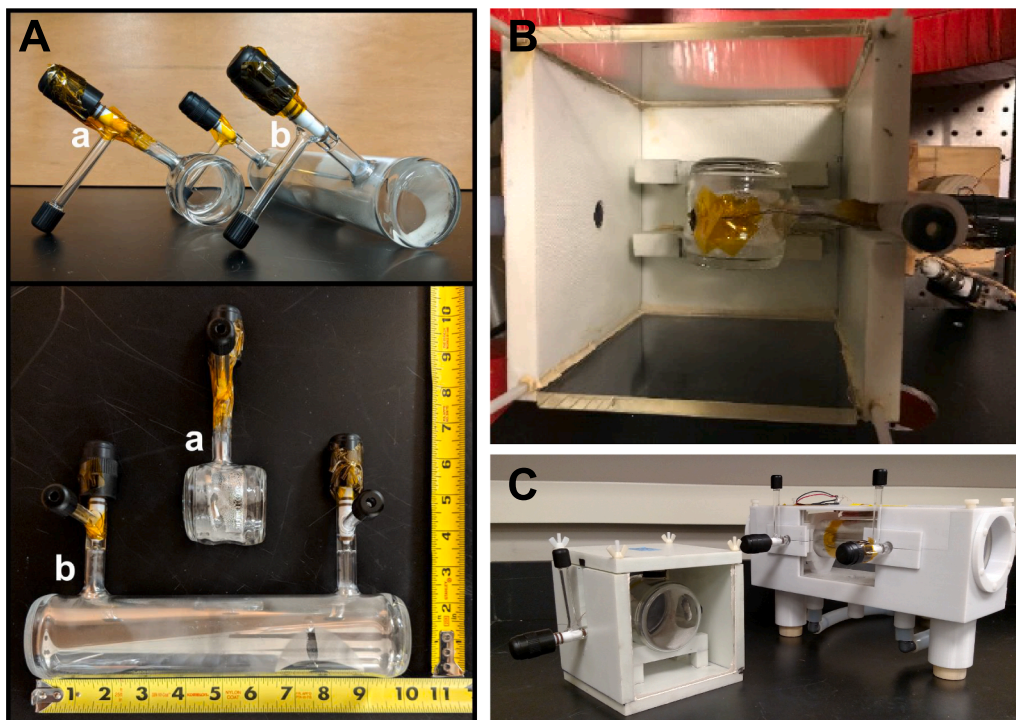


**Fig. 1.** (A) Front and top views of a 2'' × 2'' cell (a) used in this work; a 2'' × 10'' (0.5 L) cell (b) typically used in our  $^{129}\text{Xe}$  hyperpolarization experiments is shown for comparison. (B) A 2'' × 2'' cell mounted in the Garolite oven. (C) Assembled Garolite (left) and 3D-printed polycarbonate (right) forced-air ovens, containing 3'' × 3'' and 2'' × 10'' cells, respectively.

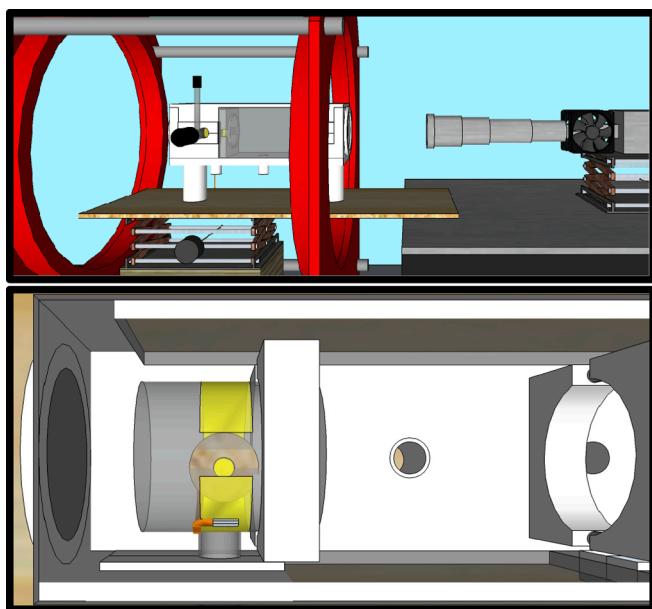


**Fig. 2.** (Top) CAD drawing of the SEOP apparatus, here with the 2'' cell (gray cylinder) mounted in the polycarbonate 3D-printed forced air oven (white) and a QPC laser with mounted beam-expanding/ polarizing optics (silver, right). The HC pair is shown in red. (Bottom) Top-view close-up of the interior of the 3D-printed oven, showing the 2'' cell mounted near the rear, in the most homogeneous region of the magnetic field. A thermocouple (orange wire) is mounted above the stem with Kapton tape (yellow); the surface detection coil is shown as beneath the transparent cell. A retro-reflecting mirror is mounted within the rear wall of the oven (dark gray, left).

### 3.2. Modeling $^{131}\text{Xe}$ spin relaxation to obtain spin-exchange rates

Extracting  $\gamma_{SE}$  values from  $^{131}\text{Xe}$  polarization dynamics is confounded by the inability to independently measure  $\Gamma_{Xe}$  (131) and its large size relative to  $\gamma_{SE}$  (compared to the case of  $^{129}\text{Xe}$ ). Guided by previous efforts [21,23,22,24–27,30,53–55], we constructed a model of gas-phase  $^{131}\text{Xe}$  relaxation (see SI document for more details). Following Anger et al.'s formulation for  $^{129}\text{Xe}$  [55], we may also write for  $^{131}\text{Xe}$ :

$$\Gamma_{Xe} = \Gamma_t + \Gamma_p + \Gamma_w \quad (2)$$

$$= \alpha[\text{Xe}] + \beta(B_0, T)\chi'_{Xe} + \Gamma_w, \quad (3)$$

where  $\Gamma_t$ ,  $\Gamma_p$ , and  $\Gamma_w$  are the contributions from transient (binary) Xe-Xe collisions, persistent Xe-Xe dimers (the three-body term), and wall collisions, respectively;  $\alpha$  and  $\beta$  are the corresponding relaxation rate constants from transient and persistent Xe dimers,  $[\text{Xe}]$  is the xenon density in amagats, and  $\chi'_{Xe}$  is effectively a Xe “reduced mole fraction”:

$$\chi'_{Xe} = \frac{[\text{Xe}]}{[\text{Xe}] + r[\text{N}_2]}, \quad (4)$$

where  $r = 0.51$  is a ratio quantifying the relative efficiency with which  $\text{N}_2$  breaks up persistent Xe-Xe dimers compared to that of Xe itself (assuming our binary gas mixture, and that the  $\text{N}_2$   $r$  value is the same for  $^{131}\text{Xe}$  as  $^{129}\text{Xe}$  [55]).

For  $^{129}\text{Xe}$ ,  $\Gamma_t$  and  $\Gamma_p$  are dominated by the spin-rotation interaction, with a  $\Gamma_p$  contribution coming from chemical-shift anisotropy (CSA). Whereas  $\Gamma_t$  depends on  $[\text{Xe}]$ ,  $\Gamma_p$  is independent of  $[\text{Xe}]$  and instead depends on the mixture's Xe fraction.  $\Gamma_w$  arises from dipolar interactions between  $^{129}\text{Xe}$  and surface spins and is not expected to have a dependence on  $[\text{Xe}]$ , but should be proportional to the container's surface-to-volume ratio (S/V) and have an exponential temperature dependence.

Unlike  $^{129}\text{Xe}$ ,  $^{131}\text{Xe}$  spin relaxation is dominated by interactions between the nucleus's quadrupole moment and local electric field

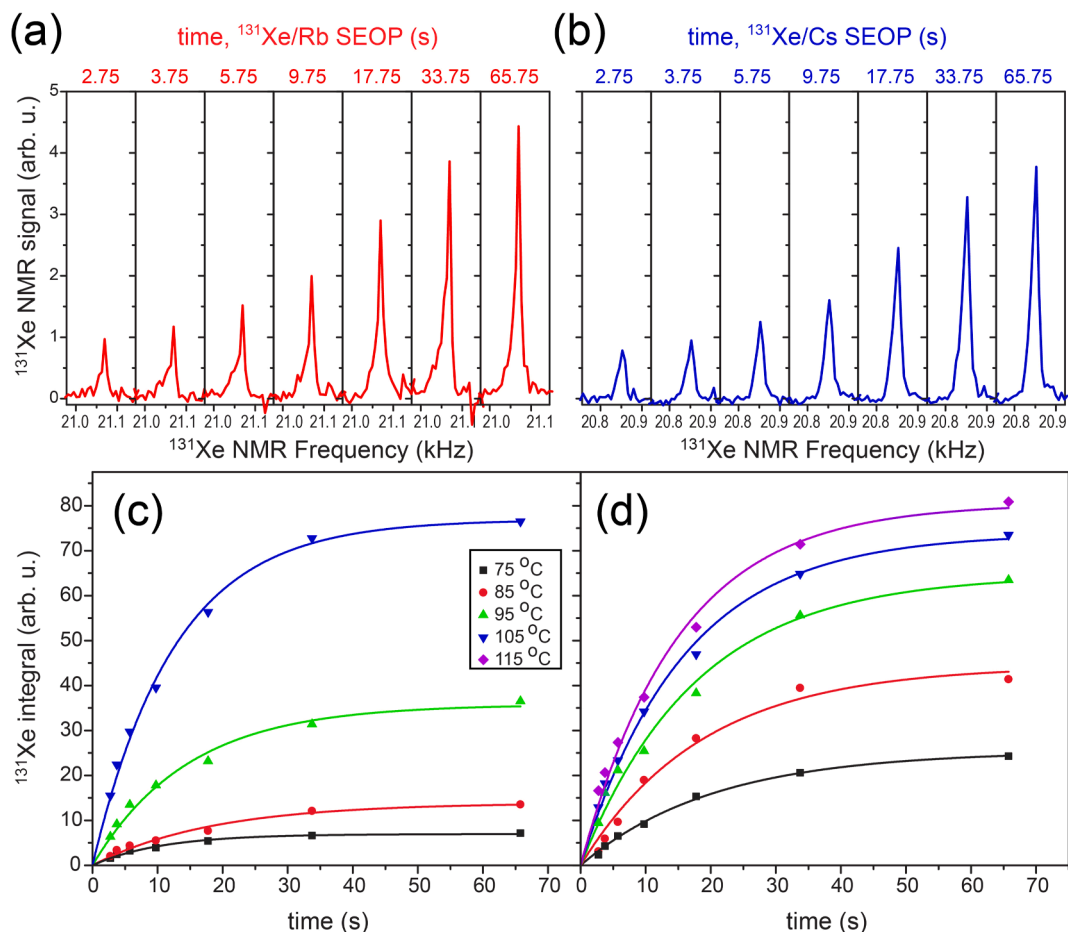


**Fig. 3.** (a,b) Single-scan *in situ* low-field  $^{131}\text{Xe}$  NMR spectra acquired at 20.9 kHz, 105 °C at each delay time ( $\tau$ ) for Rb (a) and Cs (b). Here,  $\tau$  values are fixed delay times between the re-zeroing of the  $^{131}\text{Xe}$  magnetization and the NMR signal acquisition for a given data point; specific values are given at the top of (a,b). (c,d)  $^{131}\text{Xe}$  polarization dynamics curves from SEOP with Rb (c) and Cs (d) generated by fitting the integrated  $^{131}\text{Xe}$  NMR signal (average of 24 scans, see SI document) at each  $\tau$  to the exponential function:  $S(t) = S_0[1 - \exp(-t\Gamma_{SEOP})]$ .

gradients. Nevertheless, their fluctuations are modulated by the same types of collisions, giving rise to the same overall contributions in Eq. 2—albeit with far greater rates. For  $\Gamma_t = \alpha[\text{Xe}]$ ,  $\alpha$  is  $3.96 \times 10^{-2} \text{ s}^{-1}$ , giving a  $^{131}\text{Xe}$   $T_1$  of only 68 s from that contribution alone at 300 torr Xe (0.37 amagat) [21,59], compared to hours for  $^{129}\text{Xe}$ . We also assume that  $\Gamma_w(131)$  will be independent of gas mixture [55] but will have the same qualitative dependence on  $T$  and  $S/V$  as  $\Gamma_w(129)$  [22,23]. Accordingly, we also expect that  $\beta$  will depend on  $T$  and  $B_0$  (but will be independent of  $[\text{Xe}]$  [23])—such that faster relaxation contributions will likely be observed at higher fields and lower temperatures. To obtain estimates for  $\Gamma_p$  and  $\Gamma_w$ , we examined  $\Gamma_{Xe}(131)$  measurements [23] with varying Xe fraction. Subtraction of  $\Gamma_t$  allows the residual relaxation rate to be plotted as a function of  $\chi'_{Xe}$  (see SI document), and values of  $\beta=0.140$  and  $\Gamma_w=0.0302 \text{ s}^{-1}$  were obtained for  $T = 290 \text{ K}$ ,  $B_0=9.4 \text{ T}$  from a linear fit. Data from [23] obtained during SEOP, combined with  $^{131}\text{Xe}$  surface relaxation measurements [22] modeled with an Arrhenius temperature dependence, allowed extrapolation of  $\Gamma_p$  and  $\Gamma_w(T)$  to our conditions, giving  $\beta=0.036$  and  $\Gamma_p=\beta\cdot\chi'_{Xe}=2.4 \times 10^{-2} \text{ s}^{-1}$  (Fig. 2(a)). Under our conditions (and unlike often with  $^{129}\text{Xe}$ ), the “intrinsic” ( $\Gamma_p+\Gamma_t$ ) contributions are predicted to dominate, and  $\Gamma_w$  can be negligible;  $\Gamma_w$  can become significant when  $S/V$  is much larger,  $T$  is lower, and/or the surface adhesion energy is larger (e.g. with hydrophobic surfaces) [22,23].

Subtraction of  $\Gamma_{Xe}(131)$  from  $\Gamma_{SEOP}$  values in Fig. 4(a) permitted corresponding spin-exchange rates ( $\gamma_{SE}$ ) with  $^{131}\text{Xe}$  to be estimated for each alkali metal and at each temperature (Fig. 4(b)). Over this

temperature range, the spin-relaxation rate is predicted to be nearly flat, whereas the spin-exchange rate should increase exponentially with  $[\text{AM}]$ . In principle (and as discussed in the SI document), this analysis can be taken a further step by plotting such  $\gamma_{SE}$  values versus the density for each alkali metal  $[\text{AM}]$  to yield an effective  $^{131}\text{Xe}/\text{AM}$  spin-exchange cross-section ( $\gamma'$ ) for each case [47]. However, the easiest way to change the alkali metal vapor density is to change the temperature, and this approach tends to neglect any other temperature-dependent contributions to the dynamics. Moreover, such an approach is further complicated here by: (1) the fact that the present data does not have direct measurements of  $[\text{AM}]$ , requiring instead that the  $[\text{AM}]$  values be estimated from literature vapor-pressure curves [60]; and (2) the deviations from linear  $\gamma_{SE}$  behavior over the entire temperature range (Fig. 4(b)—particularly the lowest-temperature point with Rb<sup>2</sup>). Thus, such results should be treated only as rough estimates. Doing so yields values of  $\gamma'(\text{Rb}/^{131}\text{Xe}) \sim 5 \times 10^{-15} \text{ cm}^3 \cdot \text{s}^{-1}$  and  $\gamma'(\text{Cs}/^{131}\text{Xe}) \sim 1-2 \times 10^{-15} \text{ cm}^3 \cdot \text{s}^{-1}$  respectively. These values are discussed in greater detail in the SI

<sup>2</sup> While the Rb/ $^{131}\text{Xe}$  75 °C data set did have the lowest SNR, the origin of its anomalous behavior is unclear. Although higher  $\Gamma_{Xe}(131)$  rates (and hence, total  $\Gamma_{SEOP}$  values [24,22]) are indeed expected at lower temperatures (tending to endow a shallow, asymmetric ‘u-shape’ to such graphs), neither the point’s large absolute value nor its difference from the corresponding point in the Cs data set can be explained by the  $\Gamma_{Xe}(131)$  temperature dependence. One possible explanation could arise from an unexpectedly high AM density (e.g. possibly owing to direct laser heating of Rb during that earlier run).

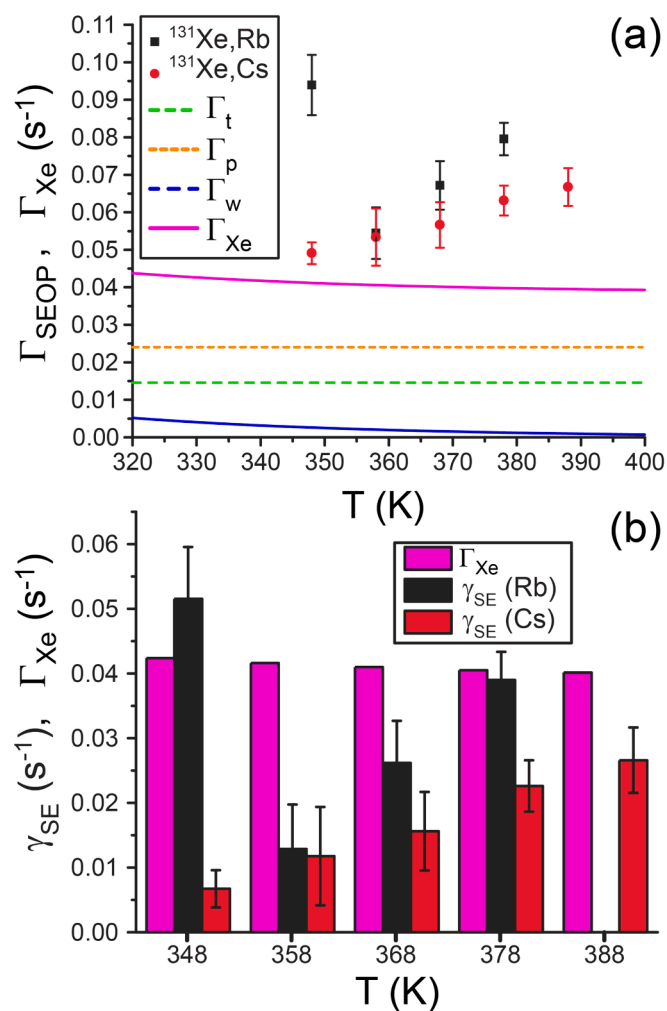


**Fig. 4.** (a)  $^{131}\text{Xe}$  SEOP rate constants,  $\Gamma_{SEOP}$ , versus temperature for both Rb/Xe (black) and Cs/Xe (red); estimated  $^{131}\text{Xe}$  spin relaxation contributions are plotted for comparison (see SI document). (b)  $^{131}\text{Xe}$ /Rb (black) and  $^{131}\text{Xe}$ /Cs (red) spin-exchange rates ( $\gamma_{SE}$ ), after subtraction of the estimated contributions from  $\Gamma_{Xe}(131)$  (magenta) from the SEOP rate constants plotted in (a). Error bars are uncertainties from the curve fits in Fig. 3.

document, but are in rough agreement with expectation based on no more than a few-fold reduction in spin-exchange for  $^{131}\text{Xe}$  compared to  $^{129}\text{Xe}$ . Indeed, as shown in Fig. 4(b), the  $^{131}\text{Xe}$  spin-exchange rates for both Cs and Rb under our conditions appear to be high enough to compete with  $^{131}\text{Xe}$  auto-relaxation and allow significant  $^{131}\text{Xe}$   $P_{Xe}N$  values—even at relatively high Xe densities.

### 3.3. Measurements of $^{131}\text{Xe}$ nuclear spin polarization

Determining the absolute  $^{131}\text{Xe}$  polarization  $P_{Xe}$  from this first dataset was confounded by the large difference in gyromagnetic ratios for  $^{131}\text{Xe}$  versus the thermally polarized reference ( $^1\text{H}$  in water). Indirect comparisons through a third nucleus (HP  $^{129}\text{Xe}$ ) allowed  $P_{Xe}$  to be initially estimated at  $\sim 1$ –10%. To measure  $P_{Xe}$ , a second set of experiments was performed using the Rb cell. First, measurements of the  $^{131}\text{Xe}$  NMR signal as a function of laser wavelength found that the polarization was generally higher when the laser centroid was red-shifted from the Rb D1 absorption maximum (Figs. 5(a,b))—consistent with previous  $^{129}\text{Xe}$  results when using a spectrally narrowed laser in the power-limited regime [61]. Lower-than-expected  $^{131}\text{Xe}$  signals—despite the higher RF frequency (46 kHz) and elevated cell temperatures compared

to the first dataset—were found to result from Rb loss from the cell's optical region, giving greatly reduced spin-exchange rates (see SI document). The cell was then washed and used as a secondary thermally polarized water reference, allowing its matched geometry to reduce systematic errors in  $P_{Xe}$ . The ability to detect NMR signals from HP  $^{131}\text{Xe}$  and  $^1\text{H}$  from thermally polarized water at the same frequency (at  $\sim 13$  and  $\sim 1.1$  mT, respectively) allowed  $P_{Xe}$  to be measured as a function of offset wavelength (Fig. 5) and cell temperature (Fig. 5(c)), with  $P_{Xe}$  peaking at  $2.17\% \pm 0.39\%$  for this second dataset.

Measurements of other relevant systematics (see SI document) determined  $P_{Xe}$  values from the first dataset (Fig. 5(c)). Under conditions for the dynamics experiments in Fig. 3,  $P_{Xe}$  values of up to  $3.4 \pm 0.7\%$  and  $3.8 \pm 0.7\%$  were measured for Rb/Xe and Cs/Xe SEOP, respectively. Even greater values were measured under higher-temperature conditions of “Rb runaway” [4,62,63] wherein laser heating causes positive feedback with Rb density, reaching values as high as  $P_{Xe} = 7.6\% \pm 1.5\%$ . This value corresponds to a  $\geq 10^2$ -fold improvement in  $P_{Xe}N$  over previous efforts.

To help achieve these results, key improvements in our experiment have included: (1) using high-powered, spectrally narrowed laser sources, which dramatically increased the resonant photon flux (by roughly an order of magnitude or more); (2) *in situ* low-field NMR detection, which allowed the SEOP conditions to be found that gave the greatest  $^{131}\text{Xe}$  polarization; (3) using a “square cylinder” (i.e. length = diameter) cell, a design which not only minimizes a cylinder's S/V ratio—mitigating surface-induced  $^{131}\text{Xe}$  relaxation—but its shallow

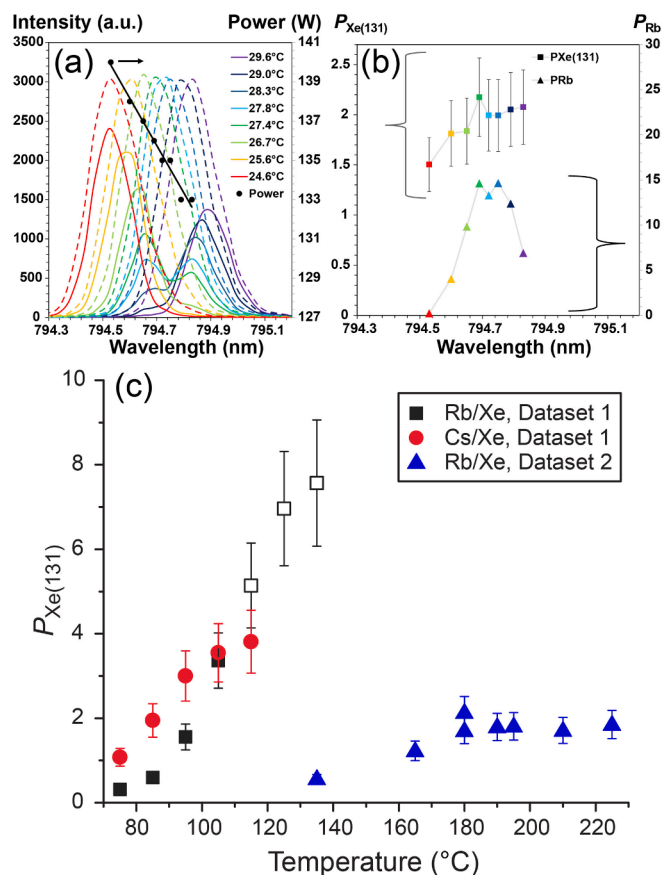


**Fig. 5.** (a) Near-IR spectra for the SEOP laser transmitted through the Rb cell when at room temperature (dotted) and at 180 °C (with magnet on, solid lines) as the laser is tuned by varying the LDA temperature, as well as corresponding power measurements (black circles/line). (b)  $P_{Xe}$  (squares) and Rb polarization values (triangles, estimated from laser transmission variations with field cycling [7]) for each laser centroid wavelength. (c) Absolute  $P_{Xe}$  values as a function of cell temperature for both datasets; open icons are single-point acquisitions taken under conditions of “Rb runaway”.

depth also provided better through-cell illumination; and (4) use of a rich (50%) Xe gas mixture with enriched  $^{131}\text{Xe}$  but low (<1 atm) total pressure. Indeed, many of these features acted synergistically to further improve the  $^{131}\text{Xe}$  polarization. For example, we note that the use of enriched  $^{131}\text{Xe}$  was enabling for these experiments, as it helped provide sufficient detection sensitivity for real-time *in situ* low-field NMR for  $^{131}\text{Xe}$  SEOP optimization; however, it directly accounted for only a factor of  $\sim 4$  of the overall improvement in  $P_{Xe}N$ . Moreover, the high resonant laser flux permitted operation at relatively high  $^{131}\text{Xe}$  density but low total pressure (obviating the need to further pressure-broaden the alkali metal absorption line); combined with the shallow cell depth, it also allowed SEOP at higher temperatures, providing illumination to achieve sufficient alkali metal polarization at higher alkali metal densities (increasing the spin-exchange rate) while further minimizing surface-induced  $^{131}\text{Xe}$  relaxation. Finally, while it is expected that higher cell temperatures should improve Xe polarization (to a point [63]), *in situ* NMR allowed us to find our highest  $^{131}\text{Xe}$  polarization values under conditions of “Rb runaway”, an unexpected result—particularly since such conditions are generally considered detrimental to  $^{129}\text{Xe}$  SEOP [4,62,63].

To improve this experiment, employing a metal heating jacket should enable more stable SEOP control at high cell temperatures [64]. Moreover, given that these experiments are almost certainly photon-limited, further improvements in  $P_{Xe}N$  should be possible with higher incident laser powers—particularly when combined with better temperature control.

#### 4. Conclusion

We have optimized SEOP to polarize  $8.5 \times 10^{20}$   $^{131}\text{Xe}$  nuclei to  $7.6\% \pm 1.5\%$ , a  $\geq 10^2$ -fold improvement in  $P_{Xe}N$  over previous efforts. Such a value of  $P_{Xe}N$  is large enough to conduct a sensitive search for TRIV in neutron- $^{131}\text{Xe}$  scattering and has already enabled the first measurement of neutron- $^{131}\text{Xe}$  pseudomagnetic precession [43]. These results may inspire further improvements in SEOP polarization of other quadrupolar noble gas isotopes (e.g.  $^{83}\text{Kr}$  [42] and  $^{21}\text{Ne}$  [65]), with applications ranging from medical imaging to searches for CPT/Lorentz violation. Higher  $P_{Xe}N$  using more laser power delivered over larger volumes will benefit neutron TRIV searches, the motivations and prospects of which are discussed in greater detail in the SI. Another intriguing potential application is pulmonary imaging with HP  $^{131}\text{Xe}$ , with its surface-selective relaxation potentially providing orthogonal contrast to that of HP  $^{129}\text{Xe}$  as shown for HP  $^{83}\text{Kr}$  [42]. However, before such biomedical applications can be realized, a number of technical challenges must first be overcome. First, while the present  $P_{Xe}N$  levels might be sufficient for low-resolution studies in small-animal models, they would likely need to be increased by over an order of magnitude for human studies. Next, whereas the envisioned neutron-science applications would likely involve probing the HP  $^{131}\text{Xe}$  within its SEOP cell, for biomedical applications it would of course have to be transferred to the subject. Unlike the case with HP  $^{129}\text{Xe}$ , HP  $^{131}\text{Xe}$  cannot be cryocollected, as the  $^{131}\text{Xe}$   $T_1$  in condensed phases is generally on the ms timescale [23] (which would also preclude direct observation of dissolved-phase resonances); moreover, as discussed above the  $^{131}\text{Xe}$   $T_1$  is generally short even in the gas phase. In the previous HP  $^{131}\text{Xe}$  experiments of Meersmann et al. [23], gas samples were ejected through a filter into an evacuated container in order to allow detection of the HP gas at high field. Similarly for pulmonary imaging applications, to save time the hyperpolarizer would likely need to eject a large volume of the Xe gas mixture while hot, with an in-series alkali metal condenser that could rapidly remove all of the metal atoms while cooling the gas to enable *in vivo* administration. Lastly, the optimal SEOP conditions for  $^{131}\text{Xe}$  SEOP (temperature, gas mixture, etc.) are not the same as those for  $^{129}\text{Xe}$ , which presents challenges for hyperpolarizer design and

operation (not to mention the vastly different MR resonance frequencies for  $^{131}\text{Xe}$  versus  $^{129}\text{Xe}$ ).

Potential biomedical developments would likely benefit from further studies of differential  $^{131}\text{Xe}$  relaxation (perhaps incorporated into the relaxation model provided here) in the presence of hydrophobic versus hydrophilic surfaces—particularly in the context of lung pathologies [42]. For example, through the surface quadrupolar relaxation (SQUARE) effect [42,66],  $^{131}\text{Xe}$  may be able to detect pathological tissues through changes in surface adhesion, or highlight regions with reduced surface area (e.g. alveolar surfaces lost to COPD [66]). Near-simultaneous ventilation imaging with HP  $^{129}\text{Xe}$  may also enable ratiometric quantification of such contrast. Importantly, HP  $^{129}\text{Xe}$  was recently approved by the FDA for clinical pulmonary imaging. Given its relatively high natural abundance (21.2%), the presence of  $^{131}\text{Xe}$  in xenon gas mixtures thus offers the possibility of using HP  $^{131}\text{Xe}/^{129}\text{Xe}$  as a readily available “dual reporter” contrast agent. Towards this end, we are currently studying the feasibility of simultaneously polarizing and detecting  $^{131}\text{Xe}$  and  $^{129}\text{Xe}$  in a clinical-scale xenon hyperpolarizer [67]—efforts that will be reported in due course.

#### Declaration of Competing Interest

The authors declare that they have no known competing financial interests or personal relationships that could have appeared to influence the work reported in this paper.

#### Data availability

Data will be made available on request.

#### Acknowledgments

We acknowledge funding support from NSF (CHE-1905341, CHE-1904780, and REU funding from the NSF/DoD ASSURE Program, DMR-1757954), DoD CDMRP (W81XWH-15-1-0272, W81XWH2010578, W81XWH-15-1-0271, W81XWH-20-10576), and a Cottrell Scholar SEED Award (B.M.G., RCSA). W. M. Snow acknowledges support from US National Science Foundation grant PHY-1913789 and PHY-2209481 and the Indiana University Center for Spacetime Symmetries. M.S. Rosen acknowledges support of the Kiyomi and Ed Baird MGH Research Scholar award.

#### Appendix A. Supplementary material

Supplementary data associated with this article can be found, in the online version, at <https://doi.org/10.1016/j.jmr.2023.107521>.

#### References

- [1] T.G. Walker, W. Happer, Spin-exchange optical pumping of noble-gas nuclei, *Rev. Mod. Phys.* 69 (1997) 629–642.
- [2] B. Driehuys, G.D. Cates, E. Miron, K. Sauer, D.K. Walter, W. Happer, High-volume production of laser-polarized  $^{129}\text{Xe}$ , *Appl. Phys. Lett.* 69 (12) (1996) 1668–1670.
- [3] M.S. Rosen, T.E. Chupp, K.P. Coulter, R.C. Welsh, S.D. Swanson, Polarized  $^{129}\text{Xe}$  optical pumping/spin exchange and delivery system for magnetic resonance spectroscopy and imaging studies, *Rev. Sci. Instr.* 70 (2) (1999) 1546–1552.
- [4] A.L. Zook, B.B. Adhyaru, C.R. Bowers, High capacity production of >65% spin polarized xenon-129 for NMR spectroscopy and imaging, *J. Magn. Reson.* 159 (2) (2002) 175–182.
- [5] M.G. Mortuza, S. Anala, G.E. Pavlovskaya, T.J. Dieken, T. Meersmann, Spin-exchange optical pumping of high-density xenon-129, *J. Chem. Phys.* 118 (4) (2003) 1581–1584.
- [6] I.C. Ruset, S. Ketel, F.W. Hersman, Optical pumping system design for large production of hyperpolarized  $^{129}\text{Xe}$ , *Phys. Rev. Lett.* 96 (2006) 053002.
- [7] P. Nikolaou, N. Whiting, N.A. Eschmann, K.E. Chaffee, B.M. Goodson, M.J. Barlow, Generation of laser-polarized xenon using fiber-coupled laser-diode arrays narrowed with integrated volume holographic gratings, *J. Magn. Reson.* 197 (2) (2009) 249–254.
- [8] G. Norquay, G.J. Collier, M. Rao, N.J. Stewart, J.M. Wild,  $^{129}\text{Xe}$ -Rb spin-exchange optical pumping with high photon efficiency, *Phys. Rev. Lett.* 121 (2018) 153201.

- [9] P. Nikolaou, A.M. Coffey, L.L. Walkup, B.M. Gust, N. Whiting, H. Newton, S. Barcus, I. Muradyan, M. Dabaghyan, G.D. Moroz, et al., Near-unity nuclear polarization with an open-source  $^{129}\text{Xe}$  hyperpolarizer for NMR and MRI, *Proc. Natl. Acad. Sci. USA* 86 (2013) 14150–14155.
- [10] P. Nikolaou, A.M. Coffey, M.J. Barlow, M.S. Rosen, B.M. Goodson, E. Y. Chekmenev, Temperature-ramped  $^{129}\text{Xe}$  spin-exchange optical pumping, *Anal. Chem.* 86 (16) (2014) 8206–8212.
- [11] B.M. Goodson, NMR of laser-polarized noble gases in molecules, materials, and organisms, *J. Magn. Reson.* 155 (2002) 157.
- [12] J.P. Mugler III, T.A. Altes, Hyperpolarized  $^{129}\text{Xe}$  MRI of the human lung, *J. Magn. Reson. Imag.* 37 (2) (2013) 313–331.
- [13] D.A. Barskiy, A.M. Coffey, P. Nikolaou, D.M. Mikhaylov, B.M. Goodson, R. T. Branca, G.J. Lu, M.G. Shapiro, V.-V. Telkki, V.V. Zhivonitko, et al., NMR hyperpolarization techniques of gases, *Chem. Eur. J.* 23 (4) (2017) 725–751.
- [14] D. Bear, R.E. Stoner, R.L. Walsworth, V.A. Kostelecky, C.D. Lane, Limit on Lorentz and CPT violation of the neutron using a two-species noble-gas maser, *Phys. Rev. Lett.* 85 (2000) 5038.
- [15] F. Cane, D. Bear, D. Phillips, M. Rosen, C. Smallwood, R. Stoner, R. Walsworth, V. Kostelecky, Bound on Lorentz- and CPT-violating boost effects for the neutron, *Phys. Rev. Lett.* 93 (2004) 230801.
- [16] C. Gemmel, W. Heil, S. Karpuk, K. Lenz, Y. Sobolev, K. Tullney, M. Burghoff, W. Kilian, S. Knappe-Grüneberg, W. Müller, et al., Limit on and CPT violation of the bound neutron using a free precession  $^3\text{He}/^{129}\text{Xe}$  comagnetometer, *Phys. Rev. D* 82 (2010) 111901(R).
- [17] F. Allmendinger, W. Heil, S. Karpuk, W. Kilian, A. Scharth, U. Schmidt, A. Schnabel, Y. Sobolev, K. Tullney, New limit on Lorentz and CPT violating neutron spin interactions using a free precession  $^3\text{He}-^{129}\text{Xe}$  co-magnetometer, *Phys. Rev. Lett.* 112 (2014) 110801.
- [18] Y.V. Stadnik, V.V. Flambaum, Nuclear spin-dependent interactions: searches for WIMP, axion and topological defect dark matter, and tests of fundamental symmetries, *Eur. Phys. J. C* 75 (2015) 110.
- [19] V.A. Kostelecky, A.J. Vargas, Lorentz and CPT tests with clock-comparison experiments, *Phys. Rev. D* 98 (2018) 036003.
- [20] N. Sachdeva, I. Fan, E. Babcock, M. Burghoff, T. Chupp, S. Degenkolb, P. Fierlinger, S. Haude, E. Kraegle, W. Kilian, et al., New limit on the permanent electric dipole moment of  $^{129}\text{Xe}$  using  $^3\text{He}$  comagnetometry and SQUID detection, *Phys. Rev. Lett.* 123 (2019) 143003.
- [21] D. Brinkmann, E. Brun, H. Staub, Kernresonanz im gasförmigen Xenon, *Helv. Phys. Acta* 35 (1962) 431–436.
- [22] R. Butscher, G. Wäckerle, M. Mehring, Nuclear quadrupole interaction of highly polarized gas phase  $^{131}\text{Xe}$  with a glass surface, *J. Chem. Phys.* 100 (9) (1994) 6923–6933.
- [23] K.F. Stupic, Z.I. Cleveland, G.E. Pavlovskaya, T. Meersmann, Hyperpolarized  $^{131}\text{Xe}$  NMR spectroscopy, *J. Magn. Reson.* 208 (1) (2011) 58–69.
- [24] C. Volk, T. Kwon, J. Mark, Y. Kim, J. Woo, Measurement of the Rb-Xe  $^{131}\text{Xe}$  spin-exchange cross section in  $\text{Xe}^{131}$  relaxation studies, *Phys. Rev. Lett.* 44 (3) (1980) 136.
- [25] T. Kwon, J. Mark, C. Volk, Quadrupole nuclear spin relaxation of  $^{131}\text{Xe}$  in the presence of rubidium vapor, *Phys. Rev. A* 24 (4) (1981) 1894.
- [26] Z. Wu, W. Happer, J. Daniels, Coherent nuclear-spin interactions of adsorbed  $^{131}\text{Xe}$  gas with surfaces, *Phys. Rev. Lett.* 59 (13) (1987) 1480.
- [27] Z. Wu, S. Schaefer, G. Cates, W. Happer, Coherent interactions of the polarized nuclear spins of gaseous atoms with the container walls, *Phys. Rev. A* 37 (1988) 1161–1175.
- [28] Z. Wu, W. Happer, M. Kitano, J. Daniels, Experimental studies of wall interactions of adsorbed spin-polarized  $^{131}\text{Xe}$  nuclei, *Phys. Rev. A* 42 (1990) 2774–2784.
- [29] S. Appelt, G. Wäckerle, M. Mehring, Deviation from Berry's adiabatic geometric phase in a  $^{131}\text{Xe}$  nuclear gyroscope, *Phys. Rev. Lett.* 72 (25) (1994) 3921.
- [30] D. Rafferty, H. Long, D. Shykind, P. Grandinetti, A. Pines, Multiple-pulse nuclear magnetic resonance of optically pumped xenon in a low magnetic field, *Phys. Rev. A* 50 (1) (1994) 567.
- [31] J. Luo, X. Mao, J. Chen, S. Wang, M. Zhao, L. Fu, X. Zeng, Frequency-selective laser optical pumping and spin exchange of cesium with  $^{129}\text{Xe}$  and  $^{131}\text{Xe}$  in a high magnetic field, *Appl. Magn. Reson.* 17 (4) (1999) 587–595.
- [32] M. Bulatowicz, R. Griffith, M. Larsen, J. Mirjanian, C. Fu, E. Smith, W. Snow, H. Yan, T. Walker, Laboratory search for a long-range T-odd, P-odd interaction from axionlike particles using dual-species nuclear magnetic resonance with polarized  $^{129}\text{Xe}$  and  $^{131}\text{Xe}$  gas, *Phys. Rev. Lett.* 111 (10) (2013) 102001.
- [33] A. Vershovskii, A. Pazgalev, V. Petrov, The nature of the effect of precession-frequency mismatch between  $^{129}\text{Xe}$  and  $^{131}\text{Xe}$  nuclei under spin-exchange pumping by alkali-metal atoms, *Tech. Phys. Lett.* 44 (4) (2018) 313–315.
- [34] V.I. Petrov, A.S. Pazgalev, A.K. Vershovskii, Isotope shift of nuclear magnetic resonances in  $^{129}\text{Xe}$  and  $^{131}\text{Xe}$  caused by spin-exchange pumping by alkali metal atoms, *IEEE Sens. J.* 20 (2) (2019) 760–766.
- [35] D.A. Thrasher, S. Sorensen, J. Weber, M. Bulatowicz, A. Korver, M. Larsen, T. Walker, Continuous comagnetometry using transversely polarized Xe isotopes, *Phys. Rev. A* 100 (6) (2019) 061403.
- [36] F.P. Calaprice, W. Happer, D.F. Schreiber, M.M. Lowry, E. Miron, X. Zeng, Nuclear alignment and magnetic moments of  $^{133}\text{Xe}$ ,  $^{133}\text{Xe}^m$ , and  $^{131}\text{Xe}^m$  by spin exchange with optically pumped  $^{87}\text{Rb}$ , *Phys. Rev. Lett.* 54 (1985) 174–177.
- [37] Y. Zheng, G.W. Miller, W.A. Tobias, G.D. Cates, A method for imaging and spectroscopy using  $\gamma$ -rays and magnetic resonance, *Nature* 537 (7622) (2016) 652–655.
- [38] M. Gatzke, G. Cates, B. Driehuys, D. Fox, W. Happer, B. Saam, Extraordinarily slow nuclear spin relaxation in frozen laser-polarized  $^{129}\text{Xe}$ , *Phys. Rev. Lett.* 70 (5) (1993) 690.
- [39] G.E. Pavlovskaya, Z.I. Cleveland, K.F. Stupic, R.J. Basaraba, T. Meersmann, Hyperpolarized krypton-83 as a contrast agent for magnetic resonance imaging, *Pro. Nat. Acad. Sci. USA* 102 (51) (2005) 18275–18279.
- [40] T. Hughes-Riley, J.S. Six, D.M. Lilburn, K.F. Stupic, A.C. Dorkes, D.E. Shaw, G. E. Pavlovskaya, T. Meersmann, Cryogenics free production of hyperpolarized  $^{129}\text{Xe}$  and  $^{83}\text{Kr}$  for biomedical MRI applications, *J. Magn. Reson.* 237 (2013) 23–33.
- [41] D.M. Lilburn, G.E. Pavlovskaya, T. Meersmann, Perspectives of hyperpolarized noble gas MRI beyond  $^3\text{He}$ , *J. Magn. Reson.* 229 (2013) 173–186.
- [42] J.S. Six, T. Hughes-Riley, D.M. Lilburn, A.C. Dorkes, K.F. Stupic, D.E. Shaw, P. G. Morris, I.P. Hall, G.E. Pavlovskaya, T. Meersmann, Pulmonary MRI contrast using surface quadrupolar relaxation (SQUARE) of hyperpolarized  $^{83}\text{Kr}$ , *Magn. Reson. Imag.* 32 (1) (2014) 48–53.
- [43] H. Lu, M.J. Barlow, D. Basler, P. Gutfreund, O. Holderer, A. Ioffe, S. Pasini, P. Pistel, Z. Salhi, K. Zhernenkov, B.M. Goodson, W.M. Snow, E. Babcock, First measurement of neutron birefringence in polarized  $^{129}\text{Xe}$  and  $^{131}\text{Xe}$  nuclei, *arxiv* (2023) 2301.00460.
- [44] P. Nikolaou, A.M. Coffey, L.L. Walkup, B.M. Gust, C.D. LaPierre, E. Koehnemann, M.J. Barlow, M.S. Rosen, B.M. Goodson, E.Y. Chekmenev, A 3D-printed high power nuclear spin polarizer, *J. Am. Chem. Soc.* 136 (2014) 1636–1642.
- [45] I. Saha, P. Nikolaou, N. Whiting, B.M. Goodson, Characterization of violet emission from Rb optical pumping cells used in laser-polarized xenon NMR experiments, *Chem. Phys. Lett.* 428 (4–6) (2006) 268–276.
- [46] K. Ranta, Ph.D. thesis, Southern Illinois U. (2016).
- [47] G.D. Cates, R.J. Fitzgerald, A.S. Barton, P. Bogorad, M. Gatzke, N.R. Newbury, B. Saam, Rb- $^{129}\text{Xe}$  spin-exchange rates due to binary and three body collisions at high x pressures, *Phys. Rev. A* 45 (1992) 4631–4639.
- [48] D. Schaper, C. Auton, L. Barrón-Palos, M. Borrego, A. Chavez, L. Cole, C. Crawford, J. Curole, H. Dhahri, K. Dickerson, et al., A modular apparatus for use in high-precision measurements of parity violation in polarized eV neutron transmission, *Nucl. Instrum. Methods Phys. Res.* 969 (2020) 163961.
- [49] W. Happer, E. Miron, S. Schaefer, D. Schreiber, W.A. van Wijngaarden, X. Zeng, Polarization of the nuclear spins of noble-gas atoms by spin exchange with optically pumped alkali-metal atoms, *Phys. Rev. A* 29 (1984) 3092–3110.
- [50] R. Herman, Theory of spin exchange between optically pumped rubidium and foreign gas nuclei, *Phys. Rev.* 137 (4A) (1965) A1062.
- [51] Y.-Y. Jau, N.N. Kuzma, W. Happer, High-field measurement of the  $^{129}\text{Xe}$ -Rb spin-exchange rate due to binary collisions, *Phys. Rev. A* 66 (5) (2002) 052710.
- [52] W. Shao, G. Wang, E.W. Hughes, Measurement of spin-exchange rate constants between  $^{129}\text{Xe}$  and alkali metals, *Phys. Rev. A* 72 (2) (2005) 022713.
- [53] F.J. Adrian, Quadrupolar relaxation of  $^{131}\text{Xe}$  in xenon gas, *Phys. Rev.* 138 (2A) (1965) A403.
- [54] B. Chann, I. Nelson, L. Anderson, B. Driehuys, T. Walker,  $^{129}\text{Xe}$ -Xe molecular spin relaxation, *Phys. Rev. Lett.* 88 (11) (2002) 113201.
- [55] B. Anger, G. Schrank, A. Schoeck, K. Butler, M. Solum, R. Pugmire, B. Saam, Gas-phase spin relaxation of  $^{129}\text{Xe}$ , *Phys. Rev. A* 78 (4) (2008) 043406.
- [56] X. Zeng, Z. Wu, T. Call, E. Miron, D. Schreiber, W. Happer, Experimental determination of the rate constants for spin exchange between optically pumped K, Rb, and Cs atoms and  $^{129}\text{Xe}$  nuclei in alkali-metal–noble-gas van der Waals molecules, *Phys. Rev. A* 31 (1985) 260–278.
- [57] N. Whiting, N.A. Eschmann, B.M. Goodson, M.J. Barlow,  $^{129}\text{Xe}$ -Cs (D1, D2) versus  $^{129}\text{Xe}$ -Rb (D1) spin-exchange optical pumping at high xenon densities using high-power laser diode arrays, *Phys. Rev. A* 83 (5) (2011) 053428.
- [58] M. Kelley, R. Branca, Theoretical models of spin-exchange optical pumping: Revisited and reconciled, *J. Appl. Phys.* 129 (2021) 154901.
- [59] 1 amagat (amg) =  $2.6873 \times 10^{19} \text{ cm}^{-3}$ , equal to the number density of an ideal gas at 0 °C and 760 Torr.
- [60] D. Steck, Cesium D Line Data and Rubidium 87 D Line Data, <http://steck.us/alkalidata>, *rev. 2.2.1* (2019).
- [61] N. Whiting, P. Nikolaou, N. Eschmann, M. Barlow, R. Lammert, J. Ungar, W. Hu, L. Vaissie, B. Goodson, Using frequency-narrowed, tunable laser diode arrays with integrated volume holographic gratings for spin-exchange optical pumping at high resonant fluxes and xenon densities, *Appl. Phys. B* 106 (4) (2012) 775–788.
- [62] C. Witte, M. Kunth, F. Rossella, L. Schröder, Observing and preventing rubidium runaway in a direct-infusion xenon-spin hyperpolarizer optimized for high-resolution hyper-CEST (chemical exchange saturation transfer using hyperpolarized nuclei) NMR, *J. Chem. Phys.* 140 (8) (2014) 084203.
- [63] P. Nikolaou, A.M. Coffey, K. Ranta, L.L. Walkup, B.M. Gust, M.J. Barlow, M. S. Rosen, B.M. Goodson, E.Y. Chekmenev, Multidimensional mapping of spin-exchange optical pumping in clinical-scale batch-mode  $^{129}\text{Xe}$  hyperpolarizers, *J. Phys. Chem. B* 118 (2014) 4809–4816.
- [64] J.R. Birchall, P. Nikolaou, A.M. Coffey, B.E. Kidd, M. Murphy, M. Molway, L. B. Bales, B.M. Goodson, R.K. Irwin, M.J. Barlow, et al., Batch-mode clinical-scale optical hyperpolarization of xenon-129 using an aluminum jacket with rapid temperature ramping, *Anal. Chem.* 92 (6) (2020) 4309–4316.
- [65] R.K. Ghosh, M.V. Romalis, Measurement of spin-exchange and relaxation parameters for polarizing  $^{21}\text{Ne}$  with K and Rb, *Phys. Rev. A* 81 (4) (2010) 043415.
- [66] D. Lilburn, C. Lesbats, J. Six, E. Dubuis, L. Yew-Booth, D. Shaw, M. Belvisi, M. Birrell, G. Pavlovskaya, T. Meersmann, Hyperpolarized  $^{83}\text{Kr}$  magnetic resonance imaging of alveolar degradation in a rat model of emphysema, *J.R. Soc. Interface* 12 (2015) 20150192.
- [67] J.R. Birchall, R.H. Chowdhury, P. Nikolaou, Y.A. Chekmenev, A. Scherbakov, M. J. Barlow, B.M. Goodson, E.Y. Chekmenev, Pilot quality-assurance study of a third-generation batch-mode clinical-scale automated xenon-129 hyperpolarizer, *Molecules* 27 (2022) 1327.